1. AGENCY USE ONLY (Leave blank)	2. REPORT DATE 31 Mar 95	3. REPORT TYPE AND DATES COVERED final 30 Sep 93 through 31 Mar 95

4. TITLE AND SUBTITLE Fracture Mechanics of Advanced Composites (DEPSCoR 92)	5. FUNDING NUMBERS G F49620-93-1-0550

6. AUTHOR(S)
Michael C. Larson

AFOSR-TR-95

0684

7. PERFORMING ORGANIZATION NAME(S) AND ADDRESS(ES)

Department of Mechanical Engineering
Tulane University
New Orleans, LA 70118-5674

9. SPONSORING / MONITORING AGENCY NAME(S) AND ADDRESS(ES)

AFOSR/NA
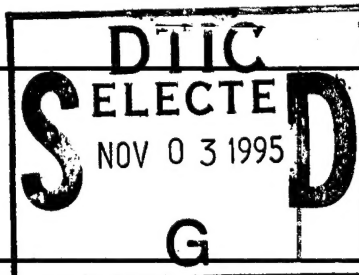110 Duncan Avenue Suite B115
Bolling AFB, DC 20332-0001

10. SPONSORING / MONITORING AGENCY REPORT NUMBER

19951027 098

11. SUPPLEMENTARY NOTES

12a. DISTRIBUTION / AVAILABILITY STATEMENT

unlimited

DTIC SELECTED NOV 0 3 1995 G

12b. DISTRIBUTION CODE

DTIC QUALITY INSPECTED 5

13. ABSTRACT (Maximum 200 words)

This report documents instrumentation obtained under a DEPSCoR grant to support research in the mechanics of advanced composite materials. While the equipment will support a broad range of research topics, it has already spawned studies into micromechanical fracture of advanced composite materials and nondestructive evaluation of cracked bodies. Specifically, a laser interferometry system (including optical and vibration isolation components with image processing hardware and software), and a tensile substage for an electron microscope, form the core of an experimental program which complements analytical and computational investigations.

Progress is being made in two particular areas. The first of these is the development of a coupled experimental and computational methodology for solving inverse fracture problems using laser holographic interferometry. The methodology can be utilized in the fracture mechanics of homogeneous and heterogeneous media to determine the location, size, and geometry of an embedded crack given the measured displacement history of a free surface. The technique will be valuable as a research tool for those interested in tracking the development and propagation of cracks inside test specimens. The second program involves examining microscale sliding and debonding at fiber-matrix interfaces. This study relies upon the SEM tensile substage and related equipment.

14. SUBJECT TERMS Fracture, Inverse Problem, Holographic Interferometry	15. NUMBER OF PAGES 13
	16. PRICE CODE

17. SECURITY CLASSIFICATION OF REPORT UNCLASSIFIED	18. SECURITY CLASSIFICATION OF THIS PAGE UNCLASSIFIED	19. SECURITY CLASSIFICATION OF ABSTRACT UNCLASSIFIED	20. LIMITATION OF ABSTRACT UL

FINAL REPORT

for the period September 30, 1993 through March 31, 1995
Grant Number **F49620-93-1-0550**

Fracture Mechanics of Advanced Composites

(DEPSCOR 92)

Michael C. Larson
Department of Mechanical Engineering
Tulane University
New Orleans, LA 70118
voice: (504)865-5775
fax: (504)865-5345
email: larson@me.tulane.edu

Accesion For

NTIS CRA&I	☒
DTIC TAB	☐
Unannounced	☐
Justification	

By _____

Distribution /

Availability Codes

| Dist | Avail and / or Special |
| A-1 | |

submitted to:
Contracting Officer
AFOSR/PKA
110 Duncan Avenue
Suite 115
Bolling AFB, DC 20332-0001

Contents

Publications describing investigations which utilize the equipment
obtained under this grant.

I. Overview

The equipment obtained under this grant is supporting broad research in applied mechanics and has already spawned studies into micromechanical fracture of advanced composite materials and nondestructive evaluation of cracked bodies. Specifically, a laser interferometry system (including optical and vibration isolation components with image processing hardware and software), and a tensile substage for an electron microscope, form the core of an experimental program which complements mature analytical and computational investigations.

Significant progress has already been made on two particular research projects made possible by this grant. The appendix includes copies of publications generated from the initial stages of experimentation in both investigations. The first of these is the development of a coupled experimental and computational methodology for solving inverse fracture problems. This program hinges on the laser holography equipment. The methodology can be utilized in the fracture mechanics of homogeneous and heterogeneous media to determine the location, size, and geometry of an embedded crack given the measured displacement history of a free surface. The technique will be valuable as a research tool for those interested in tracking the development and propagation of cracks inside test specimens. The second program involves examining microscale sliding and debonding at fiber-matrix interfaces. This study relies upon the SEM tensile substage and related equipment.

In addition to these initiatives currently underway, the equipment is flexible enough to provide avenues for a wide variety of mechanics studies. For example, the high sampling rate of the laser holographic system will permit the evaluation of the dynamic fracture behavior of composites, the nature of surface cracks, and multi-site damage in composite panels. The 1000 lb tensile substage for the SEM will allow monitoring of the micromechanical behavior of a wide range of materials, including metal matrix composites, polymer matrix composites, and organic and inorganic structures occurring in nature. We are currently completing a project in the biomimetics of fatigue and fracture.

II. Equipment Acquired

This section contains a list of the research equipment purchased with the funds provided by grant number F49620-93-1-0550. As stated in the letter that was sent to you on July 11,1994 regarding an extension request, the Electronic Speckle Pattern Interferometry (ESPI) system that was specified in the proposal was no longer being sold. The components that were necessary to build a similar system with some additional features are presented in an itemized list under the ESPI heading.

ELECTRONIC SPECKLE PATTERN INTERFEROMETRY SYSTEM $41823

ITEM	QUANTITY	VENDOR
photographic plate holder	3	Jodon
holographic plates	3	Jodon
rubber tank w/floating cover	3	Calumet Photographic
optical power meter and detector	1	Newport
actuator and controller	1	Newport
TI 123 CCD camera	3	Symco
25mm lens	3	Symco
computer	2	Gateway 2000
LG-3 frame grabber w/4 source cable	1	Scion
LabVIEW software	1	National Instruments
GPIB board	1	National Instruments
ConceptVi Level 2 imaging software	1	G T F S
breadboard (1'x2')	1	Newport
support posts for breadboard	1	Newport
two-stage translation stage	1	Edmund Scientific
translation stage	1	Newport
damped rod w/rack	2	Newport
rod w/rack	6	Newport
rod clamp	4	Newport
portable air compressor	1	Newport
pressure transducer	1	DCI Instruments
digital pressure gauge	1	DCI Instruments
top beam steering accessory	4	Newport
bottom beam steering accessory	2	Newport
variable beamsplitter	1	Newport
beamsplitter	2	Newport
compact spatial filter	2	Newport
pinhole aperture (5 microns)	2	Newport
elliptical mirror	7	Newport
Pyrex mirror (1" dia)	2	Newport
mirror (2" dia)	2	Newport
mirror mount	3	Newport
mirror/beamsplitter mount	3	Newport
objective mount	2	Newport
objective (60x)	4	Newport
riser block	7	Newport
base plate	7	Newport
rotatable platform	2	Newport
laboratory jack	5	Newport
screw kit	2	Newport

STABILIZED HeNe LASER w/POWER SUPPLY $6584

ITEM   VENDOR
35mW laser   Spectra-Physics

VIBRATION ISOLATION TABLE w/SUPPORTS $7954

ITEM   VENDOR
vibration isolation table   Newport
vibration isolators   Newport

OPTICS $1775

ITEM   VENDOR
zoom microscope w/base and post   Edmund Scientific
Sony C350 camera   Edmund Scientific
rack and pinion movement   Edmund Scientific
BNC to BNC cable   Edmund Scientific

1000 lb TENSILE SUBSTAGE $6300

ITEM   VENDOR
tensile substage w/extended travel   Edmund Scientific

LOAD READOUT SYSTEM $3095

ITEM   VENDOR
load readout system   Ernest Fullam

MOTOR DRIVE SYSTEM $2000

ITEM   VENDOR
motor drive system   Ernest Fullam

III. Appendix

INVERSE ANALYSIS FOR EMBEDDED FRACTURES

William D. Keat* and Mark J. Halliday†
Clarkson University
Potsdam, New York

Michael C. Larson‡ and Melody L. Arthur§
Tulane University
New Orleans, Louisiana

Abstract

A coupled computational and experimental investigation was undertaken to assess the feasibility of a procedure for subsurface crack identification based on inspection and/or inversion of surface displacements. The study began with the linear problem of generating contour maps of the surface deformations produced by buried fractures of known geometry and loading. An indirect boundary element formulation using the fundamental solution for tensile and shear multipoles near a half-space provided an efficient mathematical representation of the 3-D fracture. These preliminary results offered evidence for the existence of unique correspondences between crack geometry (and loading) and the resulting uplift at the free surface. The inverse problem of crack identification was then addressed beginning with the development of a hybrid of the Marquardt-Levenberg algorithm. Numerical and physical experiments were conducted to assess robustness of the proposed inversion methodology. The experimental medium was a cube of transparent brittle material in which a fracture was hydraulically pressurized. Displacements induced at the surface of the specimen were measured by laser interferometry and compared to numerical results.

Introduction

This paper examines the feasibility of a nondestructive evaluation tool based on using measurements of surface deformations to estimate the geometry of a three-dimensional embedded fracture. Potential applications range from the tracking of underground hydraulic fractures to laboratory monitoring of crack growth in test specimens and the nondestructive inspection of structural components under in-service loading.

---

*Assistant Professor, Mechanical and Aeronautical
  Engineering
.†Graduate Student, Mechanical and Aeronautical
  Engineering
‡Assistant Professor, Mechanical Engineering
§Graduate Student, Mechanical Engineering

The proposed methodology fits the standard definition of an inverse problem[1]. Uniqueness of the solution is therefore a central issue. In fact, there are an infinite number of fracture geometries that may be associated with a given surface deformation pattern. Therefore constraints have to be placed on the set of allowable geometries in a manner consistent with the underlying physics. Furthermore, any computational strategy must be robust enough to deal with the noise levels arising from the following sources: model approximations of material behavior, uncertainty in the boundary conditions, and errors in the experimental measurements. The other issue concerns the efficiency of the inversion algorithm. The latter must consist of two parts: a model of the three-dimensional fracture near a free surface, and a nonlinear equation solver. If either one proves to be excessively inefficient, it could render the completed algorithm impractical.

Because the very nature of the inverse problem relies on processing measured data, surface displacements in this case, a comprehensive methodology must synthesize an analysis capability for interpreting measurements with an experimental data gathering technique. Practical inputs to the inverse solution procedure will be subject to the stoichiometric considerations which necessarily accompany any metrological endeavor. Using inputs generated by a computer code to validate a computational methodology's utility as a practical analysis tool would be a dubious undertaking. In order to reveal the worth of an inverse solver as a useful tool for researchers and technicians, one must demonstrate the accuracy by inputting actual measurements and comparing the results with known solutions.

The following paper describes progress made towards developing a coupled computational and experimental technique for solving inverse problems related to fracture mechanics of homogeneous and heterogeneous materials.

Fracture Model

To be suitable for the inverse problem, a fracture model must be both efficient and general. For example,

Mellings and Aliabadi[2] employed a dual boundary element method to study the inverse problem in two dimensions. Those endeavoring to solve the inverse problem in three dimensions have mainly focused on deriving appropriate analytical solutions. By necessity, fracture models of this type tend to be restricted to only the simplest of geometries, which in many cases precludes the possibility of finding a solution with a high level of confidence. A strategy holding far greater promise is to derive the displacement influence functions for infinitesimal fracture events such as the multipole. These are applicable to a broader range of geometries when incorporated in an integral equation formulation. A fairly complete summary of the various 3-D solutions can be found in a paper by Okada[3]. In some instances they have been applied to investigate the inverse problem[4].

The fundamental solution for point forces near a planar bimaterial interface, derived by Rongved[5] in terms of Papkovitch functions, served as the starting point for deriving the displacement fundamental solution for tensile and shear multipoles in a semi-infinite region[6]. The Papkovitch functions were differentiated twice, first with respect to the field point coordinates in accordance with the following classical elasticity equation relating the Papkovitch functions, $\bar{B}^k$ and β^k, to the displacement components, u_i^k:

$$u_i^k = B_i^k - \frac{1}{4(1-v)}\left[B_i^k + r_j \frac{\partial B_j^k}{\partial x_i} + \frac{\partial \beta^k}{\partial x_i} \right] \qquad (1)$$

where the superscript k indicates the direction of the applied force and v is Poisson's ratio. A second set of derivatives was taken with respect to the source point coordinates consistent with multipole definitions for opening and shear:

$$u_i = -hP_1\left\{ n_k n_j u_{i,j}^k + \left(\frac{v}{1-v}\right)\left(s_k s_j + t_k t_j\right)u_{i,j}^k \right\}$$
$$\quad - hP_2\left\{ \left(s_k n_j + n_k s_j\right)u_{i,j}^k \right\} \qquad (2)$$
$$\quad - hP_3\left\{ \left(t_k n_j + n_k t_j\right)u_{i,j}^k \right\}$$

where $\bar{n}$, $\bar{s}$, and $\bar{t}$ form an orthogonal triad of local basis vectors oriented with $\bar{n}$ normal to the crack plane; hP_1 is the intensity of the opening mode (or tensile) multipole; hP_2 and hP_3 are the intensities of two shear multipoles which are superimposed onto the tensile multipole to fully represent a fracture event of infinitesimal extent.

The displacements induced at a field point on the free surface can be found by summing the effects of the multipoles acting over the crack surface, S_C. If expressed in terms of components of relative displacement δ_j (i.e. crack opening, dip, and slip) which are related to the multipole intensities through Hooke's law, the following integral equation results:

$$u_i = \iint_{S_c} \Gamma_{ij}^D \, \delta_j \, dA \qquad (3)$$

where Γ_{ij}^D are the displacement-influence coefficients derived in equation (2). The integral is nonsingular for embedded fractures and thus can be evaluated by Gauss quadrature. Note that the key feature of this *surface integral method* is that only the surface of the fracture needs to be discretized.

Demonstration results have been presented in Figure 1 for planar and nonplanar fracture geometries.
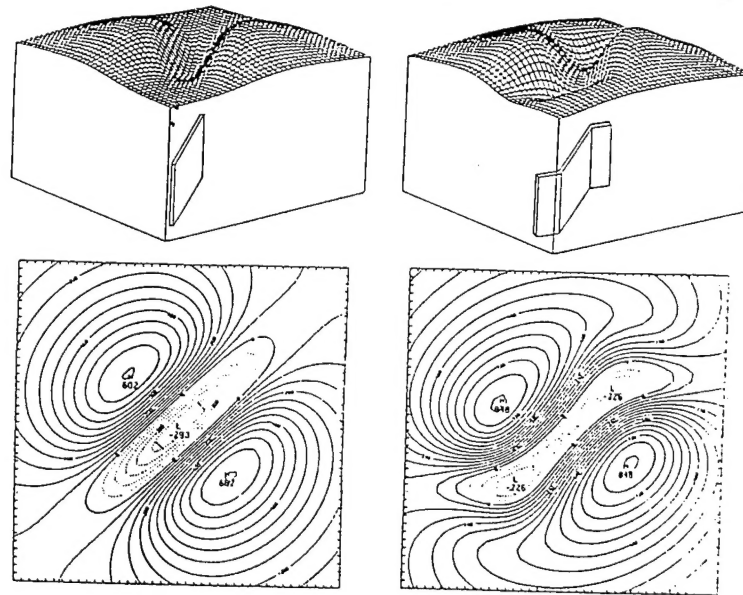

Figure 1. Sample surface and contour plots of vertical displacement for a planar fracture and a doubled-angled vertical crack.

Two types of graphical representations have been employed to represent vertical displacements (w) at the free surface: the vertical heights of points lying on the 'surface plots' are proportional to the value of w; 'contour plots' present the same results as lines of constant w. Results are characterized by a trough (or depression) along a line approximating where the kinked fracture plane intersects the free surface. In general, the trough will lie directly above the edge of the crack when the fracture is perpendicular to the free surface, and will disappear below the free surface as the parallel orientation is approached.

Inversion Algorithm

The determination of fracture geometry and location from experimental measurements of surface displacement is formulated as a nonlinear least squares problem. This is a logical choice since inherent errors, associated with the experimental observations and with restrictions imposed on the fracture geometry, serve to make an exact solution highly improbable. The scalar function to be minimized is given by:

$$R(x) = \{R\}^T\{R\} = \sum_{i=1}^{m}\left[w(x, y_i) - w_{\exp}(y_i)\right]^2 \quad (4)$$

where x is the vector of unknown parameters defining the fracture geometry; $\{R\}$ is the residual vector; w and $w_{\exp}$ are theoretical and experimental values, respectively, of the surface displacement component which is perpendicular to the free surface; y_i are coordinates defining the location of the ith measurement site on the free surface. Only the w component of surface displacement has been retained here due to limitations on the current experimental setup.

The nature of the proposed application required the development of a numerical algorithm with the capability to solve both small and large residual problems. Following in the footsteps of Dennis et al.[7,8], a classical Marquardt-Levenberg strategy has been combined with a secant approximation to secure at least superlinear convergence in the neighborhood of the global minimum.

To begin the derivation of the governing matrix equation, the usual statement of the Newton method is rewritten to take advantage of the special structure of the least-squares equations:

$$\left(J_k^T J_k + S_k\right)p_k = -J_k^T R_k \quad (5)$$

where J_k is the Jacobian matrix, S_k is the Hessian matrix, p_k is the search vector being solved for, and R_k denotes the residual vector. All quantities have been defined for the kth iteration. At the conclusion of each iteration, the vector of unknown fracture parameters (x_k) is updated by adding in the search vector as below:

$$x_{k+1} = x_k + p_k \quad (6)$$

The analytical evaluation of the derivatives required for J_k and S_k is all but impossible due to the complexity of the displacement-influence functions Γ_{ij}^D and the use of numerical integration procedures with equation (3). Furthermore, the use of standard finite difference formulae is an extraordinarily expensive proposition in terms of CPU, and in the case of S_k is prohibitively expensive. Thus for small residual problems it is both reasonable and advantageous to neglect S_k.

The resulting Gauss-Newton formulation guarantees a descent direction but does not assure a function decrease as over-shooting may occur. To overcome such problems, Levenberg[9] proposed the following modified form:

$$\left(J_k^T J_k + \mu_k I\right)p_k = -J_k^T R_k \quad (7)$$

where I is the identity matrix and μ_k is a scaling factor. As the value of μ_k is increased, the length of the search vector decreases and it direction approaches the negative gradient (as per the method of steepest descent). Numerical implementations of equation (7) have been proposed; the most popular of these is the Marquardt-Levenberg algorithm[10]. The solution of equation (7) was carried out using a QR algorithm in order to avoid the numerical instabilities associated with the normal equations solution of small residual problems. The least-squares problem is therefore cast in the following matrix form:

$$\begin{bmatrix} J_k \\ \sqrt{\mu_k}\,I \end{bmatrix}\{p_k\} = \begin{Bmatrix} R_k \\ 0 \end{Bmatrix} \quad (8)$$

When applied to small residual versions of the fracture problem, the Marquardt-Levenberg algorithm exhibited the expected q-quadratic convergence and was consistently robust[6].

However, with large residual problems the solution progressed at such a slow rate, that modifications seemed in order. Moré's[11] trust region strategy did not seem to provide a solution because, though robust, it is still essentially a small residual algorithm. The best of the remaining choices was to adopt one of several available secant approximations to S_k. The original Newton formulation is once again modified to:

$$\left(J_k^T J_k + A_k + \mu_k I\right)p_k = -J_k^T R_k \quad (9)$$

where A_k represents an approximate S_k. The recommendation of Dennis et al.[7,8], regarding the selection of A_k, is to choose a matrix which is symmetric, does not require the computation of any second derivatives, and approaches zero as the residual approaches zero.

The presence of A_k in equation (9) leads to some confusion over how to apply the QR algorithm in order to obtain a solution. A relationship equivalent to equation (8) can be established but it requires the Cholesky decomposition of A_k. This does not appear to be a viable approach, because the positive definiteness of A_k has not been enforced and a perturbed decomposition would only tend to corrupt the estimate of S_k. It is not clear how Dennis et al. (1981) resolved this issue. The solution adopted here was to solve the normal equations directly using LU decomposition. In the event that the residual becomes very small, whereupon the normal equations solution runs the risk of going unstable, the algorithm switches back to equation (7) and its more reliable QR solution procedure.

Robustness of the Inversion Algorithm

Numerical studies were conducted to assess the range of applicability of the inverse algorithm. Existence of a unique global minimum was promoted in these studies by constraining the fracture to be planar, elliptical in shape, and of constant crack opening. In Keat[6] it was demonstrated that the inversion code will converge rapidly for both large and small residual

problems while allowing for up to seven degrees of freedom (e.g. angles of orientation, spatial position, aspect ratio of the fracture, crack opening). Recent emphasis is on: (1) defining, as precisely as possible, the range of geometries that will lead to convergence to the correct global minimum and (2) the sensitivity of the converged solution to errors in both the measurement system and the model approximation.

For the constrained set of fracture geometries under consideration, the following independent parameters were identified as having a significant impact on whether or not convergence would occur: number of degrees of freedom, nearness of the starting guess to the converged solution, nondimensional crack depth, ratio of crack depth to laser-scanned surface width, number of measurement sites on scanned free surface, and systematic and random errors associated with experimental measurements.

Sample results from a parametric study which was undertaken to isolate the effects of each of these variables are given in Figures 2 and 3. In generating both sets of results, the only fracture-defining variable that has been allowed to change is the crack depth. The perpendicular orientation of the test geometry with respect to the planar free surface, the other spatial coordinates, the radius of the circular crack front, and the magnitude of crack opening have all been held fixed.

Figure 2 shows how bad the starting guess for depth can be and still lead to convergence. The abscissa displays the crack depth corresponding to the exact solution; the ordinate gives the lower limit on the set of starting guesses for crack depth that lead to convergence. It is interesting to note that the ratio of the limit starting guess to corresponding actual crack depth
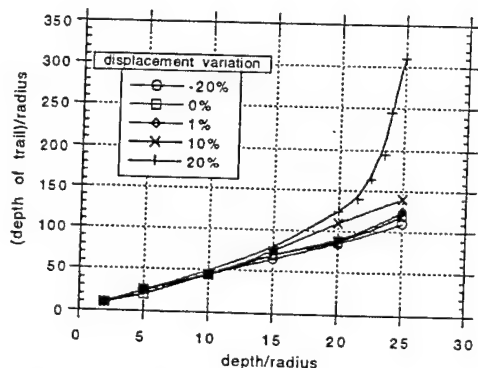

Figure 2. This plot shows the maximum depth for an initial trial solution that will converge. The constant variation in surface displacements (bias) is given in percent of the maximum dispacement for a reference crack with a nondimensional depth of 2.
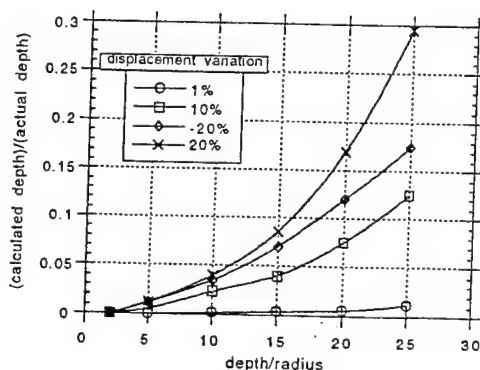

Figure 3. This plot shows the error in the calculated crack depth when a systematic bias is applied to the surface displacements. As in Figure 2, the constant bias is referenced to the maximum displacement for a crack with a nondimensional depth of 2.

remains essentially constant over the range of depths examined. Furthermore, this ratio is invariant with respect to the systematic error (or bias) for small biases. Not shown is the dependence of the limit starting guess on the ratio of crack depth to scanned surface width.

Figure 3 shows the sensitivity of errors in the converged solution to systematic errors associated with the field point measurements. The systematic error (or bias), which might for example correspond to a rigid body movement of the measured object, was introduced by adding a uniform displacement field to all the field point measurements. Percentage biases are referenced to the largest surface displacement produced by the fracture model at a nondimensional crack depth of 2. Results indicate that for nondimensional crack depths of less than 20, the percentage error observed in the converged solution is less than the percentage error introduced in the surface displacements.

Laser Interferometry Measurement System

The preliminary focus of the experimental phase of this project was to induce an internal fracture of known geometry and loading within a medium and to measure the displacement field induced on one of its free surfaces. The specimen under observation was a transparent cube of polymethyl metacrylate. Cast inside each specimen was a waxed plastic film cut to the desired crack shape which forms an area with a predilection for fracture formation.

The thin aluminum disc was mounted on the end of a fluid feed tube which was embedded in the acrylic. A penny-shaped pre-crack was formed by attaching a 6.4 centimeter diameter piece of plastic to the bottom of the 5.1 centimeter diameter aluminum disc using tape. In addition to providing a secure hold on the plastic while the acrylic is curing, this adhesive tape prevented acrylic from clogging the tube. A high pressure pump connected to the fluid feed tube supplied internal pressure to the pre-cracked area. This configuration allowed the predetermined crack to be uniformly pressurized as water was slowly forced down the feed tube.

The out-of-plane displacement field on a surface normal to this penny-shaped fracture is on the order of magnitude of micrometers. The method chosen to measure these small out-of-plane displacements is holographic interferometry. Whereas devices such as strain gauges and extensometers would be able to detect average displacements over finite, discrete lengths, holographic interferometry uses the interference of light to measure displacements continuously over the entire surface. Furthermore, this non-invasive method can resolve deformations on the order of nanometers without introducing external mechanical loading or contacting the surfaces of the specimen.

In the holographic interferometric technique employed, two laser beams, one that illuminates the surface of the specimen and one that serves as a reference, interfere with one another on a recording medium to form an image of the specimen. When two such images, i.e. one of a specimen in its undeformed state and one in its deformed state, are reconstructed on the same hologram, a fringe pattern will appear. This pattern is indicative of the amount and type of motion suffered by the test specimen between the first and second exposure of the holographic medium.

The displacement vector of an arbitrary point on the surface of the object is a simply a function of the optical phase difference, ϕ. Considering that beams of light travel in wave field that are sinusoidal in nature, the optical phase difference is the variance in phase at which two beams intersect on the recording medium. It follows form Huygen's Principle of Superposition that when two light beams of equal magnitude traveling in phase with one another interfere, the irradiance is doubled. On the other hand, if one beam lags behind the other by one half of the wavelength, it destructively interferes with the first such that no light is visible. Quantitatively, the phase difference between the beams, or wave fields, is

$$\phi = \left(\frac{2\pi}{\lambda}\right)(k_2 - k_1)L = \left(\frac{2\pi}{\lambda}\right)K \cdot L \qquad (10)$$

where λ is the wavelength of light, L is the displacement vector, K is the sensitivity vector, and k_1 and k_2 are unit vectors along the direction of viewing and illumination, respectively.

The optical arrangement for evaluating the surface contours of the acrylic test specimen is depicted in Figure 4. A 35 mW helium neon laser provided light at a wavelength of 632.8 nanometers. The light was divided with a variable beam splitter into a reference and
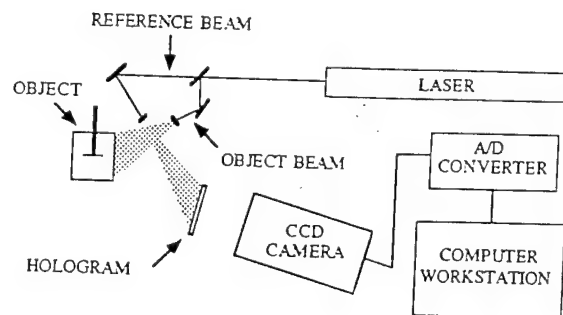

Figure 4. Holographic apparatus and image acquisition system.

an object path. Along both paths the beams were reflected and spread via use of mirrors and spatial filters. These beams were recombined on a 4 x 5 inch glass plate which sat in a micropositionable plate holder. A capture board then grabbed the images viewed through a CCD camera and transferred them to a computer for image processing.

The viewing and illumination vectors were perpendicular to one another and were oriented such that the surface normal of the specimen bisects them. Thus the sensitivity vector, K, was reduced to single component normal to the surface.

The surface of the acrylic specimen was painted white to reflect diffusely the laser light through the holographic plate and create an original image of the surface that appears bright. As the object deformed, the light reflected from each point on its surface traveled a slightly different distance than when taking the original image. If the distance was altered by half the wavelength of the laser light, this corresponding point viewed through he hologram will change from bright to dark. Substitution of π radians (one half wavelength) for ϕ in equation (10) suggests that neighboring dark fringes have a difference in out-of-plane displacements of 224 nanometers.

The pre-cracked specimen and the optical components were secured to a vibration isolation table to eliminate erroneous fringes stemming from background excitations. A specimen holder ensured that there would be no rigid body motion during pressurization.

Before supplying pressure to the test specimen, a holographic exposure of the original surface was taken and the plate was developed. After carefully repositioning the plate in its holder, the CCD camera began transferring images at thirty frames per second to the computer bus. The first frame captured contained the holographic image of the specimen in its undeformed state; the ensuing frames were holographic images of the specimen at subsequent levels of internal pressurization. The camera was oriented such that each picture contained a holographic image of the deforming surface as well as a digital display of the corresponding pressure applied to the pre-cracked region. The procedure allowed the pressure to the specimen to be steadily increased while recording a history of the fringes as they develop and evolve into different shapes. Monitoring fringes as they originate, relocate, or disappear from the surface provides a means for tracking the order of the fringes.

To evaluate a displacement contour of the surface for a chosen internal pressure, the displacement field corresponding to the initial, unpressurized holographic image of the test specimen was subtracted. Because the plate holder is only micropositionable, realigning the developed plate to a sensitivity in the submicron region is not achievable. Therefore, while readjustments to the plate's position in the holder was made to eliminate almost all of the fringes, a few remained. Fringes induced by pressurization evolved from the initial pattern. Tracking fringes from the image corresponding to the undeformed state to its new position at some applied pressure yielded the developing deformation field of the specimen surface.

Preliminary Experimental Findings

Figure 5 shows a sample comparison between an experimentally determined out-of-plane displacement field with a computationally generated prediction. This particular correlation is precursory in that it was conducted to ascertain whether the computational algorithm generates results which are compatible with
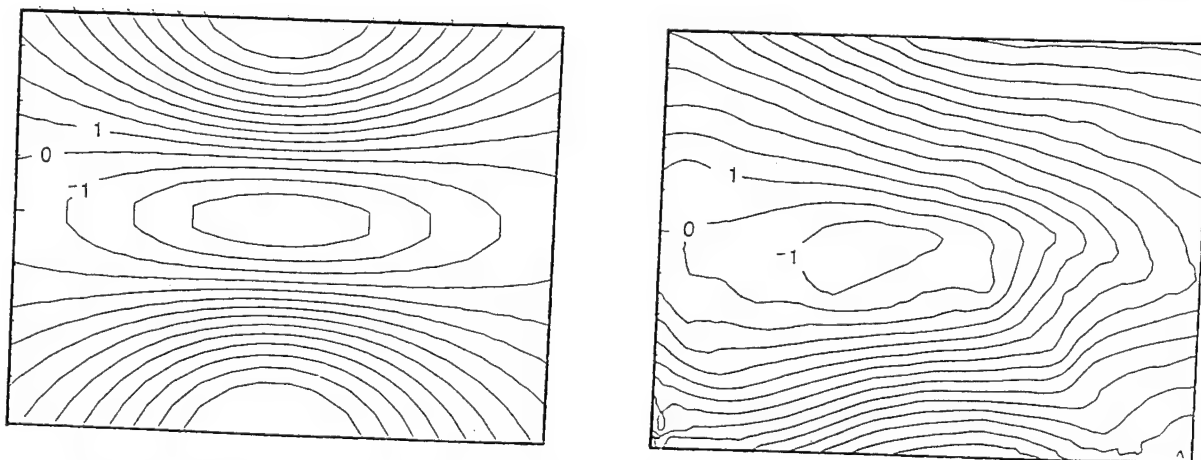

Figure 5. These contour plots show lines of constant out-of-plane displacement over the surface of a test specimen. The plot on the left represents the computational results and the one on the right the actual measurements for a surface perpendicular to the embedded penny shaped fracture. The computational contours were generated using the influence funtions for a half-space. Each contour on the left plot corresponds to 0.01 μm while the contours on the right are in 0.1 μm increments.

those yielded from the experimental measurements.

The experimental field is noticeably asymmetrical for this test case. This is tied to the manner in which the pre-crack was embedded into the specimen. As indicated earlier, a thin waxed film was attached to the disk on the end of the fluid feed tube using double-sided tape. The tape did not release uniformly during pressurization and hence led to an asymetrical crack opening distribution within the fracture. This problem is being remedied by eliminating the film and forming the existing disk to the desired geometry.

In spite of this, one can clearly see a decided qualitative agreement between the patterns, especially in the depression centered on the crack plane flanked by steep outward crests. This comparison is particularly encouraging in light of the approximate nature of the computational model employed. The fundamental solutions for a semi-infinite half space were used which only account for one of the free surfaces of the cubic test specimen. The quantitative correspondence is expected to improve dramatically through linking the surface integral representation of the fracture with a finite element formulation. This will permit the explicit representation of the bounded geometry.

Conclusions

The results outlined here for stationary cracks lend credence to the strong possibility for developing a practical nonlinear inversion methodology for resolving subsurface damage from nondestructive surface measurements. The numerical evaluations of solution sensitivity are continuing and are guiding refinements in the experimental measurement technique. The experimental program is expanding to include observations of evolving displacement patterns associated with propagating fractures. This history dependence is being used to remedy some of the uniqueness problems associated with partially defined continuum problems.

References

1. Kubo, S., "Inverse problems related to the mechanics and fracture of solids and structures", JSME Int. J., Series I, Vol. 31, No. 2, pp. 157-166, 1988.

2. Mellings, S.C., and Aliabadi, M.H., "Crack identification using inverse analysis", Boundary Elements XV, Vol. 2: Stress Analysis, Computational Mechanics Publications, Boston, 1993.

3. Okada, Y., "Surface deformation due to shear and tensile faults in a half-space", Bulletin of the Seismological Society of America, Vol. 75, No. 4, pp. 1135-1154, 1985.

4. Davis, P.M., "Surface deformation associated with a dipping hydrofracture", J. Geophys. Res., Vol. 88, No. B7, pp. 5826-5834, 1983.

5. Rongved, "Force interior to one of two joined semi-infinite solids", Proceedings of Second Midwestern Conf. on Solid Mech., pp. 1-13, 1955.

6. Keat, W.D., Surface Integral and Finite Element Hybrid Method for the Analysis of Three Dimensional Fractures, Ph.D. thesis in the Department of Mechanical Engineering, M.I.T., 1989.

7. Dennis, J.E.,Jr., Gay, D.M. and Welsch, R.E., "An adaptive nonlinear least-squares algorithm", ACM Transactions on Mathematical Software, Vol. 7, No. 3, pp. 348-368, 1981.

8. Dennis, J.E.,Jr., Gay, D.M. and Welsch, R.E., "Algorithm 573 NL2SOL - An adaptive nonlinear least-squares algorithm [E4]", ACM Transactions on Mathematical Software, Vol. 7, No. 3, pp. 348-368, 1981.

9. Levenberg, K., "A method for the solution of certain nonlinear problems in least-squares", Quart. Appl. Math., Vol. 2, pp. 164-168, 1944.

10. Marquardt, D.W., "An algorithm for least-squares estimation of nonlinear parameters", J. Soc. Indust. Appl. Math., Vol. 11, No. 2, pp. 431-441, 1963.

11. More, J.J., "The Levenberg-Marquardt algorithm: implementation and theory", Numerical Analysis, G.A. Watson, ed., Lecture Notes in Math. 630, Springer Verlag, Berlin, pp. 105-116.

95-GT-376

MICROMECHANICAL CRACK PROPAGATION
IN NICALON FIBER TOUGHENED COMPOSITES

Nagoor Preetam and Michael C. Larson
Department of Mechanical Engineering
Tulane University
New Orleans, Louisiana

ABSTRACT

Increasing the toughness of brittle ceramics with fibers has received much attention in the last five years. Many models have been put forth to describe the various facets of cracking in these materials. The intent here is to evaluate how well a relatively simple computational representation of the crack openings for a fracture in a fibrous material predicts the crack openings actually measured in an experimental specimen. The cracks are modeled as distributions of discontinuities within a surface integral representation. The influence of the fibers are accounted for through closing tractions applied at the fracture surfaces. Experimental specimens were loaded using a tensile substage mounted in a scanning electron microscope to visually monitor the crack and damage development. Some of the physical processes associated with matrix crack-fiber interactions were also evident.

INTRODUCTION

A major driving force for developing ceramic matrix composites is the potential of fabricating materials which retain the excellent thermal and stiffness characteristics of monolithic ceramics but have enhanced fracture toughness (e.g., Chou et al., 1986). Such materials would find obvious application in high temperature engine components. There are a number of mechanisms at the microstructural level which hold promise for achieving this end, one of them being fiber reinforcement.

The fracture of fiber-reinforced ceramics is typically different from that in monolithic ceramics, which often fail by the growth of a single crack on a plane normal to the maximum principle stress. Fiber composites, on the other hand, can fail by a variety of mechanisms, depending on the fiber/matrix interfacial characteristics and the interaction between a crack front and the reinforcement. Crack deflection, fiber pull-out, matrix microcracking, crack bowing and fiber bridging have been identified as major mechanisms of toughening of fiber-reinforced ceramic matrix composites.

This work establishes a two-dimensional computational model to represent the increased toughness exhibited by a $[(0/90)_4]_s$ composite system composed of a glass matrix reinforced with nicalon fibers, subjected to uniaxial tension parallel to the 0° fiber direction, through crack opening displacement calculations. This approach is relatively simple and flexible to implement in comparison to many other two-dimensional models which have been proposed in the literature (Evans, 1990). A number of approaches have been proposed in the literature to explain the increased toughness exhibited by fiber reinforced ceramic matrix composites. These approaches are based upon various descriptions of how to account for the presence of the fibers. Common models include shear lag, load transfer, debonding, and the fiber pull-out model. The enhanced toughness of fiber-reinforced ceramic composites is believed primarily to stem from the fibers left intact in the wake of an advancing fracture. This phenomenon is known as 'bridging.' In the above models it is common to represent the bridging fibers as closing tractions appled to the crack faces (e.g., Marshal, et al., 1985, Marshal and Cox, 1987). The intent here is to see if such a simplified approach captures the proper crack opening behavior in a model composite.

COMPUTATIONAL APPROACH

Computational implementation of the two-dimensional displacement discontinuity method for fractures was popularized by Crouch (1976). The methodology involves placing displacement discontinuities along the boundaries of the region to be analyzed (in this case a crack), then solving a system of algebraic equations to find the discontinuity values that produce prescribed boundary tractions. The problem of determining the displacement fields in an elastic half-space containing an edge crack is of particular significance in this investigation since it matches the experiments conducted for verification. The following section briefly describes the two-dimensional (plane strain) formulation of the displacement

discontinuity method for homogeneous, isotropic, linearly elastic materials for semi-infinite regions.

The analytical formulation for the half space is obtained by using a procedure known as the method of images. Using this method, the solution is found in two stages. In the first stage of the analysis, an infinite body containing two line segments with constant displacement discontinuities is considered. Referring to Figure 1, one of these, in $y > 0$, represents the "actual" discontinuity while the other, in $y < 0$, represents its "image", reflected about the line y=0. This makes the shear traction $t_x = \sigma_{yx}$ vanish all along $y = 0$ due to symmetry. It can be seen from Figure 2 that the edge crack lies along the line $x = 0$. In the second stage a supplementary solution is added to make the normal traction $t_y = \sigma_{yy}$ on $y = 0$ vanish.

Here we follow the development as presented in Crouch (1976) with appropriate specialization. Coordinates ξ, ζ are related to the points in the x-y system by

$$\begin{aligned} \xi &= n(x-b)-l(y-c) \\ \zeta &= l(x-b)+n(y-c) \end{aligned} \tag{1}$$

in which l and n are direction cosines of the ζ-axis relative to the x- and y-axes and b and c are the x and y distances to the origin of the ξ-ζ system. The image coordinates ξ', ζ' are described by the transformation

$$\begin{aligned} \xi' &= n(x-b)+l(y+c) \\ \zeta' &= -l(x-b)+n(y+c) \end{aligned} \tag{2}$$

Denoting the stresses due to the actual displacement by σ_{ij}^A, those due to its image by σ_{ij}^I and those resulting from the supplementary solution by σ_{ij}^S, the complete solution for the half-plane $y \geq 0$ is:

$$\sigma_{ij} = \sigma_{ij}^A + \sigma_{ij}^I + \sigma_{ij}^S \tag{3}$$

The crack is modeled as a series of these discontinuities distributed over discrete elements. The discontinuity is divided into a certain number of elements. The effect of the number of elements on the final result will be discussed later. Also the mid-points of these elements are taken as the points where the tractions are known. The crack opening displacements δ need to be calculated. Once δ is known, the stress intensity factor can be calculated. In the present analysis, δ is taken to be a constant over each element. Since the aim is to calculate the displacements δ_1, δ_2, δ_3 ... etc. for each element, we seek to formulate the problem as a system of algebraic equations:

$$t_i = C_{ij}\delta_j \tag{4}$$

In this equation, C_{ij} are influence coefficients calculated using analytical stress relationships and t_i are the tractions at the mid-points of each element. For a monolithic material loaded uniformly in the y direction, the tractions are equal to the tensile load being applied to the specimen, i.e.

$$t_i = \sigma_{ij}n_j \tag{5}$$

where n_j is the normal to each element, defining the traction direction. The most computationally intensive phase of the solution is calculating the nonsymmetric, fully populated influence coefficient matrix.

The numerical procedure involves considering the semi-infinite body containing N crack segments across which the normal displacements are discontinuous. Let the jth segment have half-width a_j, direction cosines l_j and n_j, and midpoint coordinates x_j, y_j and the normal displacement discontinuity $\hat{\delta}_j$. The stress σ_{xx} at an arbitrary point x, y in the body due to the jth discontinuity can be computed directly from equation 3. The total stress at point x, y is given by a summation of N terms, one for each of the elemental discontinuities in the body. The total normal traction at the midpoint of the ith segment can be put in the form

$$\left(\sigma_n\right)_i = \sum_{j=1}^{N}\left[\left(C_{nt}\right)_{ij}+\left(C_{nt}'\right)_{ij}\right]\left(\hat{\delta}_t\right)_j +$$
$$\sum_{j=1}^{N}\left[\left(C_{nn}\right)_{ij}+\left(C_{nn}'\right)_{ij}\right]\left(\hat{\delta}_n\right)_j \tag{6}$$

The unprimed coefficients in the above expression are the infinite body functions while the primed coefficients represent correction terms to account for the presence of the traction-free surface.

For the present case of an edge crack perpendicular to the free surface, all the crack segments are placed end to end and oriented in the same way with respect to the global coordinate system. For this case,

$$\left(\sigma_n\right)_i = -\frac{G\hat{\delta}_\zeta}{2\pi(1-v)}[-\frac{1}{(\xi+a)}+\frac{1}{(\xi-a)}+\frac{1}{(\xi'+a)}-$$
$$\frac{1}{(\xi'-a)}+\{3y+3(\xi-c)\}[+\frac{1}{(\xi'+a)^2}-$$
$$\frac{1}{(\xi'-a)^2}]+2y(\xi-c)[\frac{2}{(\xi'+a)^3}-\frac{2}{(\xi'-a)^3}] \tag{7}$$

where ξ and ξ' are given by equations 8 and 9.

$$\begin{aligned} \xi_i &= n_j(x_i-x_j)-l_j(y_i-y_j) \\ \zeta_i &= l_j(x_i-x_j)+n_j(y_i-y_j) \,. \end{aligned} \tag{8}$$

$$\begin{aligned} \xi_i' &= n_j(x_i-x_j)+l_j(y_i+y_j) \\ \zeta_i' &= -l_j(x_i-x_j)+n_j(y_i+y_j) \,. \end{aligned} \tag{9}$$

Equation (7) is the final form of the equation used to calculate the influence coefficients in the program module.

For linear elastic bodies, the stress intensity factor, K, is a measure of the propensity for crack extension: the higher is the stress intensity factor, the greater is the tendency for the crack to advance. Although it is understood that the presence of fibers will introduce nonlinear behavior, the approach taken

here for assessing the influence of the bridging fibers is to use the crack opening displacements obtained from the procedure outlined above to calculate an effective stress intensity factor. For this we employ the asymptotic, near-tip crack opening displacement solution

$$\delta(r) = \frac{K\sqrt{r}\,\kappa}{\sqrt{2\pi}\,G} \tag{10}$$

where $\kappa = 3-4\nu$ for plane strain and $\kappa = \dfrac{3-\nu}{1+\nu}$ for plane stress, G is the shear modulus, r is the distance from the crack tip to the center of the crack element and $\delta(r)$ is the crack opening displacement.

In equation (8), r, and the corresponding $\delta(r)$ need to be chosen as close to the crack tip as practical. It is possible to explicitly incorporate the form of this asymptotic solution into the interpolation function of the elemental displacement discontinuities to form specialized crack tip elements. While this is advisable for monolithic bodies, we do not take this approach here since we do not know how the non-linearities associated with the fibers and interfaces in the crack tip process zone will affect the nature of the opening displacements. Hence, collocation point displacements are fitted to match the parabolic opening near the crack tip.

The computational approach was checked against the theoretical solution for a center crack in an infinite plate to determine heuristic rules for extracting the stress intensity factor using constant elements. A trade-off must be made given that (i) the constant elements do not capture the large deformation gradient near the tip, so the more of the crack which is considered, the better the actual opening is represented, and (ii) the asymptotic crack opening solution used to calculate the stress intensity factor breaks down as distance from the tip increases. Figure 3 shows a plot between the calculated stress intensity factor, K_{cal}, and the theoretical value, K_{th}, versus percentage of the crack used in the K_{cal} approximation. Solutions run for increasing numbers of elements, i.e. decreasing element sizes, suggest that the portion of the crack to include in the stress intensity factor calculation is between 10% and 20% of the half crack length.

Concerning the closing traction exerted by individual bridging fibers, it is likely that in actuality the magnitude increases with increasing opening displacement until the fibers break. From that point onwards the closing traction decreases until the fibers are completely pulled-out of the matrix. In the present model proposed, this cycle is represented by a constant closing traction as an approximation. This closing traction, T, exerted by the fibers is applied across the fiber sites (Figure 4) and is superimposed over the opening traction, P. The relative size of the elements which have the closing traction applied is tied to the volume fraction of fibers and to the shear resistance of the interface.

The effect of the bridging length and the closing tractions exerted by the fibers on the effective stress intensity factor of the composite is studied. The computational analysis has been extended to encompass varying volume fractions of the fibers in the composite. In the present model, a steady state assumption has been made regarding the bridging length. This means that the length by which the crack extends equals the

length of the crack behind the bridging zone over which the fibers break.

According to Budiansky and Amazigo (1989), the crack opening displacement in terms of the axial stress in the fiber is given by

$$\delta = \left(\frac{\sigma_f}{\sigma_r^2}\right)(1-f)\,g_m \tag{11}$$

where σ_f is the axial stress in the fiber, σ_r is the reference stress, f is the volume fraction of the fibers, and g_m is the critical matrix energy-release rate.

The reference stress σ_r is given by

$$\frac{\sigma_r}{E} = B\left[\frac{6f^2 E_f}{(1-f)^2 E(1+\nu_m)}\right]^{1/4}\left[\frac{g_m}{rE_m}\right]^{1/2} \tag{12}$$

where ν_m is Poisson's ratio for the composite, E is the composite modulus of elasticity, E_f and E_m are the Young's Moduli of the fiber and matrix respectively, and r is the radius of the fiber.

B is a constant and is given by

$$B = \left[\frac{2(1-f)^3}{6\,\log f + 3(1-f)(3-f)}\right]^{1/4} \tag{13}$$

Equation (11) can be used to calculate δ' by substituting σ_b for σ_f, where δ' is crack opening displacement at the back of the bridge zone and σ_b is the breaking stress of the fiber. This gives an estimate of the bridge length, when comparing δ' with the crack opening displacements, over which the closing tractions will be applied.

EXPERIMENTAL DETAILS

The substage used in the experiments permits a user to observe the effects of tensile or compressive stresses of up to 1000 lb on a relatively small test specimen mounted in an SEM chamber. This substage has a load cell and a motor drive system.

The specimens are made of a composite system which consists of a barium-magnesium aluminosilicate (BMAS) matrix that contains SiC over BN coated Nicalon fibers. The fiber coatings have been applied by a chemical vapor deposition process. Carbon is deliberately added to the BN precursor since it has been found that the carbon addition minimizes reactivity during deposition between the BN and the Nicalon fibers.

Experimental specimens were cut from a 10 x 10 cm $[(0/90)_4]_S$ BMAS glass-ceramic composite panel. The material was hot-pressed subject to a maximum temperature of 1420^0 - 1440^0 C at 6.9 MPa pressure for 5 to 10 minutes in an Argon atmosphere. Complying with the requirements of the tensile substage, the dimensions of the experimental specimens was chosen to be 3.8 cm long x 0.65 wide x 0.32 cm thick. A small notch was machined into each specimen in order to localize the damage and crack development.

During loading, all five of the specimens tested exhibited the same stages of damage evolution. Figure 5 schematically

3

TABLE 1. PREDICTIONS AND MEASUREMENTS FOR CRACK OPENING DISPLACEMENTS (COD)

Distance Behind The Crack Tip (cm)	COD (numerical) (m)	COD (experimental) (m)
0.001	1.1×10^{-6}	0.91×10^{-6}
0.005	2.0×10^{-6}	1.80×10^{-6}
0.010	3.1×10^{-6}	2.70×10^{-6}
0.017	3.8×10^{-6}	3.60×10^{-6}
0.020	4.1×10^{-6}	4.50×10^{-6}

shows the development of failure observed in the notch region for the composite. Stage one involves the formation of distributed damage in the matrix around the notch. Stage two is characterized by the formation of (usually two) microcracks emanating the notch. Finally, in stage three, one of the microscopic cracks grows into a macroscopic one. This microcrack extends in a quasi-stable manner for a period of time before dynamically traversing the specimen. During the quasi-stable extension the mechanisms of crack bridging and fiber pull-out can clearly be seen under the SEM. Figure 6 shows a photograph of the trailing edge of a bridging zone capturing the transition from bridging to pull-out.

COMPARISON WITH EXPERIMENT

The results of the numerical model are compared with the experimental results for one of the specimens tested. During the quasi-stable extension of the dominant micro-crack the crack opening displacements were recorded under the scanning electron microscope under a load of 880 N. At the instant chosen, the crack was 2.5×10^{-4} m long and subject to an opening pressure of 44 MPa.

There is a stress concentration around the notch region and hence the actual stress experienced by the crack is greater than that applied remotely to the specimen, σ_0. The stress concentration effect of the notch is approximated by

$$\sigma_{eff} = \sigma_0 \left(1 + \frac{2a}{b}\right) \tag{14}$$

where σ_{eff} is the stress in the notch region, a is the semi-major axis of the ellipse, and b is semi-minor axis of the ellipse.

Hence, σ_{eff} is the opening traction used in the calculations. Also, a nominal closing traction equal to σ_{eff} is assumed in the numerical model. The major and minor axes of the elliptic notch was measured and equation 12 used to calculate σ_{eff}. σ_{eff} was found to be 440 MPa, ten times the applied nominal stress. Equations 11 through 13 are used to calculate δ', the crack opening displacement at the back of the bridged zone. Using $E_m = 15$ GPa, $E_f = 250$ GPa, $g_m = 96$ Nm^{-1}, $\sigma_b = 2.5$ GPa, $f = 0.5$, $r = 5 \mu m$, $E = 132$ GPa, $\upsilon_m = 0.2$, δ' comes out to be 1.9×10^{-6} m. This gives an estimate of the bridge length when comparing with the crack opening displacements of the unreinforced edge crack.

Table 1 lists the experimental crack opening displacements (COD) for the edge crack in a half plane and perpendicular to the free surface as a function of the distance behind the crack tip.

Comparison of the experimental crack opening displacements with the numerical crack opening displacements reveals a fairly good match; the difference ranges from about 5% to 20%. It can be seen from Table 1 that the numerical model overestimates the crack opening displacements in comparison to the experimental crack opening displacements. The major problem encountered in interpreting the measured data was that the crack trajectory, although straight on a macroscopic scale, appears to meander across the specimen when viewed under such high magnifications. This makes it difficult to measure the experimental crack opening displacements.

CONCLUSIONS

The methodology can be used to predict the variations in crack opening profiles with the volume fraction of and the frictional resistance afforded by the fibers. This variation is presumed to dictate the propensity of fracture growth and can therefore be considered an "effective" stress intensity factor, K_{eff}. This value is used for comparision purposes only as being indicative of the severity in crack opening profiles.

Figure 7 shows the ratio of the effective stress intensity factor and that which would occur in an unreinforced material possessing no fibers but having the average composite properties, $K_{eff}/K_{no\ fiber}$, versus fiber closing traction, T/P (refer to figure 4) for an edge crack in a material system with varying volume fractions of fibers. Figure 8 shows the plot between $K_{eff}/K_{no\ fiber}$ versus l/a for varying T/P ratios for an edge crack, where l/a is the bridge length normalized by the crack length. Knowing the closing traction, we can find the effective stress intensity factor from Figure 7 for a given volume fraction of fibers. From the calculated effective stress intensity factor, the bridging length can be estimated from Figure 8 for the given T/P ratio.

It can be concluded that the present simple approach for modeling the fiber reinforced ceramic-matrix composites holds promise for accurately representing crack displacements.

REFERENCES

Amizago, J.C., and Budiansky, B., 1989, " Toughening by Aligned, Frictionally Constrained Fibers," J. Mech. Phys. Solids, Vol.37, pp. 93 - 109.

Chou et al., 1986, Composite Materials, Scientific American, Vol.254, 1986, pp. 193.

Crouch, S.L., 1976, " Solution of Plane Elasticity Problems by the Displacement Discontinuity Method," Int. J. for Num. Methods in Engg., Vol.10, pp. 301-343.

Evans, A.G., 1990, "Perspective on the Development of High-Toughness Ceramics," J. of the Am. Ceram. Soc., Vol.73, pp. 187-206.

Marshal, D.B., Cox, B.N., and Evans, A.G., 1985, "The Mechanics of Mattrix Cracking in Brittle-Matrix Fiber Composites," Acta Metal., Vol 33, p.2013.

Marshal, D.B., and Cox, B.N., 1987, "Tensile Fracture of Brittle Matrix Composites: Influence of Fiber Strength," Acta Metal., Vol 35, p.2607.
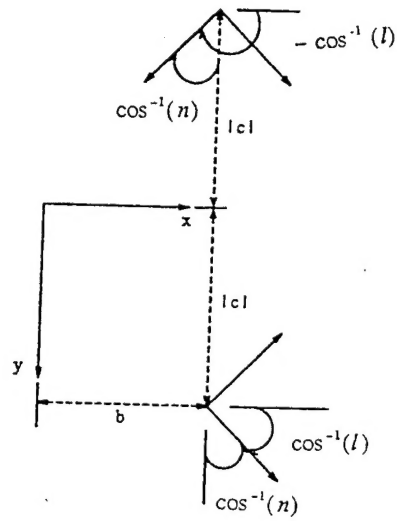
FIGURE 1. COORDINATE SYSTEMS FOR ACTUAL AND IMAGE DISPLACEMENT DISCONTINUITIES.
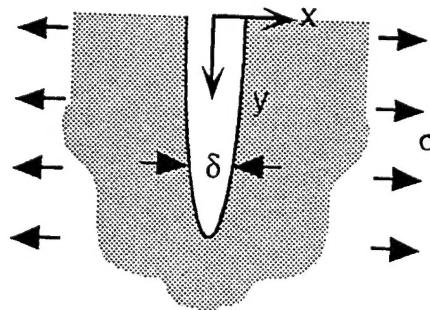

FIGURE 2. AN EDGE CRACK SUBJECT TO MODE I TENSION. THIS GEOMETRY MATCHES THE EXPERIMENTS.
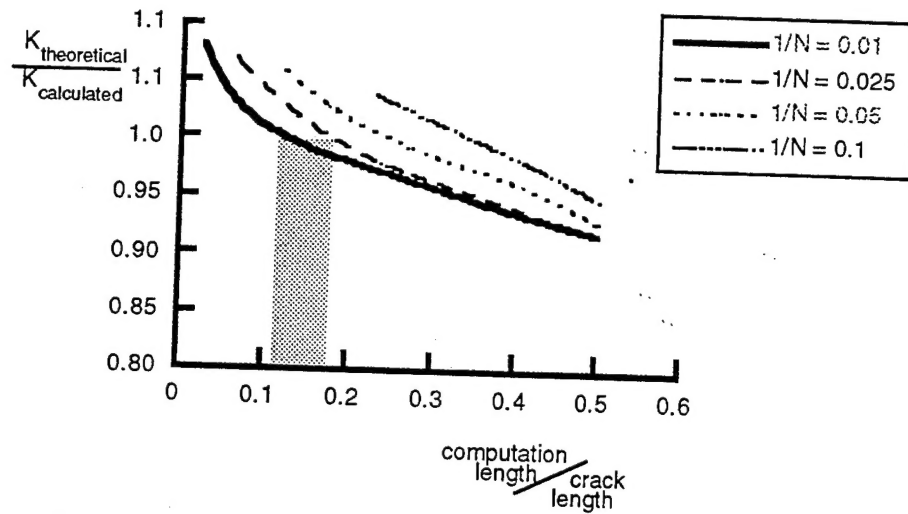
FIGURE 3. VARIATION IN THE NORMALIZED STRESS INTENSITY WITH FRACTION OF THE CRACK LENGTH USED IN THE CALCULATION. THIS SUGGESTS INCLUDING 10% TO 20% OF THE TOTAL CRACK LENGTH. (N IS THE TOTAL NUMBER OF ELEMENTS)
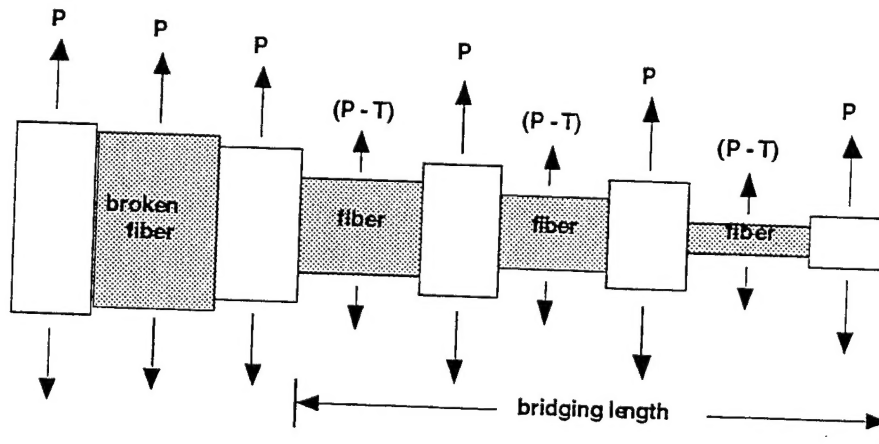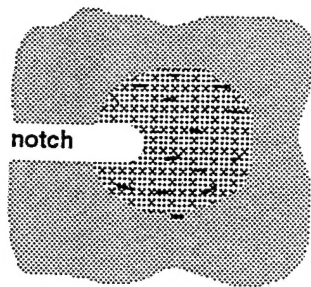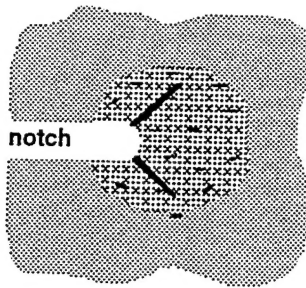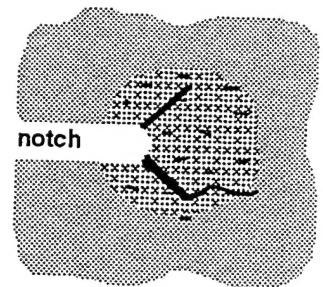

FIGURE 4. SCHEMATIC REPRESENTATION OF THE COMPUTATIONAL MODEL OF A CRACK SUBJECT TO OPENING PRESSURE, P, AND FIBER CLOSING TRACTIONS, T. THE RELATIVE ELEMENT SIZES DEPEND UPON THE FIBER VOLUME FRACTION. THE PROPORTIONS HERE SHOW 60% VOLUME FRACTION.

6

distributed damage forms
in the notch region

microcracks emanate from
the notch at about 45° off- axis

one microcrck develops into
a dominant fracture

FIGURE 5. EVOLUTION OF DAMAGE AND CRACKING OBSERVED IN THE NOTCH REGION
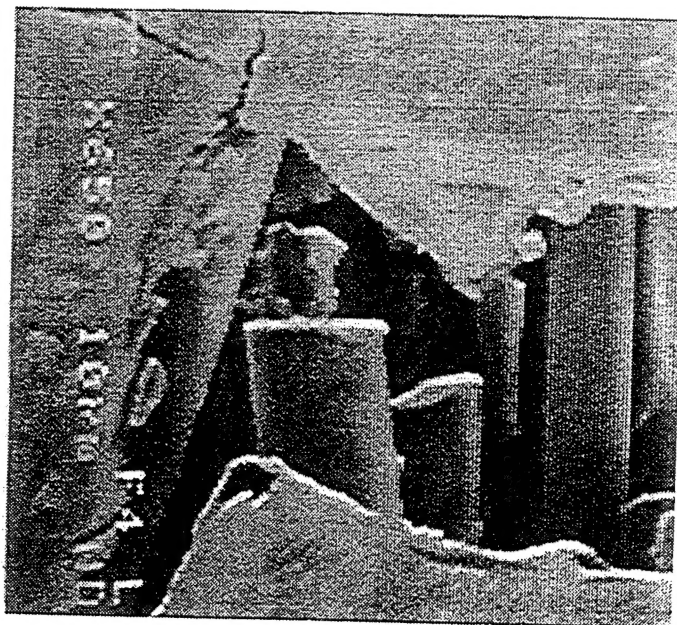OF THE EXPERIMENTAL SPECIMENS.

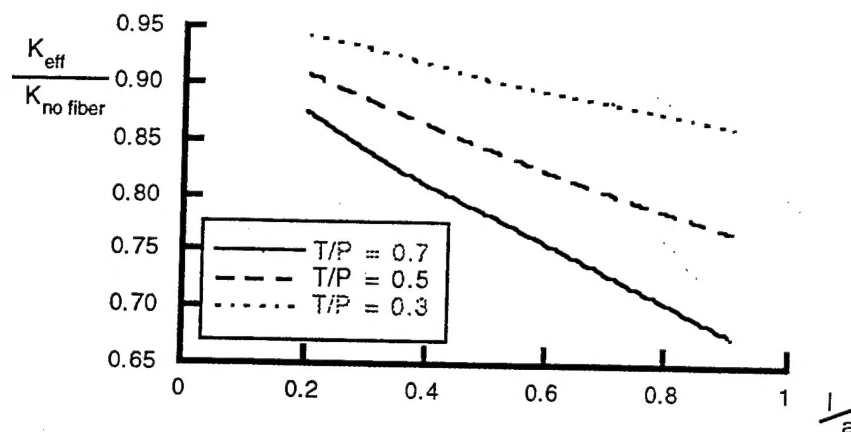FIGURE 6. REPRESENTATIVE SEM PHOTOGRAPH OF THE END OF THE BRIDGING ZONE.

FIGURE 7. COMPUTATIONAL PREDICTION OF THE VARIATION IN NORMALIZED STRESS INTENSITY FACTOR WITH THE FRACTION OF THE CRACK LENGTH BRIDGED BY FIBERS FOR THREE VALUES OF CLOSING TRACTION. ALL THE CURVES REPRESENT 50% VOLUME FRACTION OF FIBERS IN THE NICALON-GLASS COMPOSITE.
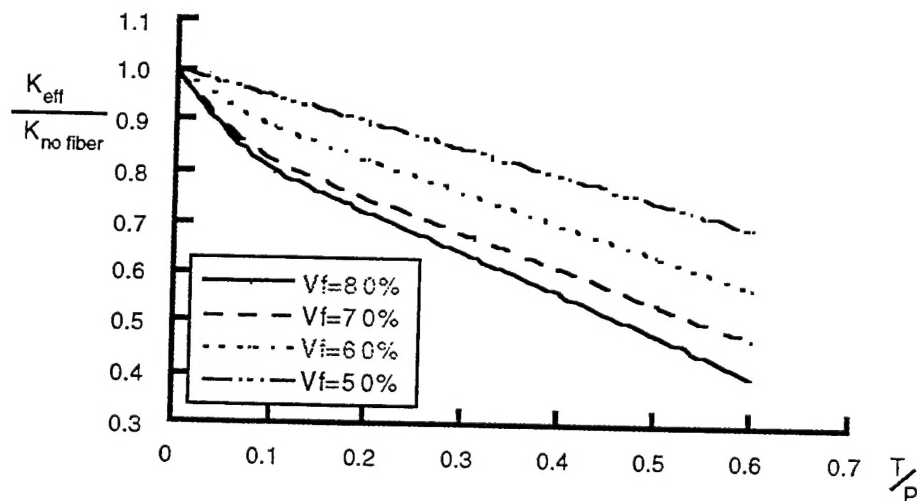

FIGURE 8. COMPUTATIONAL PREDICTION OF THE VARIATION IN NORMALIZED STRESS INTENSITY FACTOR WITH CHANGING CLOSING TRACTION FOR FOUR VALUES OF FIBER VOLUME FRACTION, Vf. ALL THE DATA REPRESENTS BRIDGING LENGTHS PREDICTED BY EQUATION 11 FOR DISPLACEMENTS CORRESPONDING TO THE FIBER BREAKING STRESS FOR THE NICALON-GLASS COMPOSITE.